JOURNAL OF CATALYSIS 144, 506–524 (1993)

Oxidation of Reduced Platinum Clusters in Pt–NaY

B. F. CHMELKA,[1,4] G. T. WENT,[2] R. CSENCSITS,[3] A. T. BELL, E. E. PETERSEN, AND C. J. RADKE[4]

Department of Chemical Engineering, University of California, Berkeley, California 94720 and Materials and Chemical Sciences Division, Lawrence Berkeley Laboratory, Berkeley, California 94720

Received August 7, 1992; revised June 14, 1993

Raman spectroscopy and ^{129}Xe NMR, in conjunction with hydrogen chemisorption and transmission electron microscopy, have been used to monitor the location and stability of metal clusters as a function of oxidation conditions for NaY-zeolite-supported platinum. After initial calcination and reduction of Pt–NaY, subsequent reoxidation at temperatures up to 873 K induces no additional agglomeration of the metal species. Different Pt–NaY systems exhibit cluster-size-dependent responses to reoxidation treatment, consistent with the greater reactivities expected for small metal particles compared to larger aggregates. We present a summary of platinum dispersal chemistry in NaY zeolite based on these and recent corroborative results.

INTRODUCTION

Preparatory treatments affect the identity and the location of metal guest species in zeolites and are, hence, crucial to the performance of zeolite-supported metal catalysts (*1–4*) and new quantum-effect materials (*5*). Homogeneous and high metal dispersion can be achieved reproducibly only through careful control of processing conditions, since migration and agglomeration of metal species can occur with subsequent loss of catalytic activity (*6–20*) or modification of material optical properties (*5, 21, 22*). Redistribution of the metal species can occur to locations either outside the crystallites' internal pore spaces or to different interior locations. Under certain conditions, metal atoms can aggregate into large low surface-area clusters on the exterior surface of micrometer-size zeolite crystallites, where the metal is poorly utilized. Metal dispersed within intracrystalline zeolite channels is highly preferred, though different interior cluster locations may be desirable depending on the intended application of a particular metal/zeolite system. For example, in optical applications, creation of quantum-confined clusters in either the supercages or in the sodalite cavities of NaY zeolite may be desirable, depending on the material bandgap properties sought. In catalytic applications, supercage sites are generally desirable for reasons of reactant accessibility (*2, 13, 17, 20, 23–25*).

To produce clusters in locations where the highly dispersed metal can be most effectively exploited, metal/zeolite preparation procedures have often relied on empirical recipes. Migratory tendencies on the part of the metal species during treatment processes are still not completely understood because the transformations undergone by metal guest species during their activation and dispersal have not been firmly established. Thus, to control metal distribution within the zeolite matrix, it is important that the detailed chemistry of the metal/zeolite preparation be better understood. A

[1] Present address: Department of Chemical and Nuclear Engineering, University of California, Santa Barbara, CA 93106.

[2] Present address: Curagen Corp., Branford, CT 06405.

[3] Present address: Argonne National Laboratory, Argonne, IL 60439.

[4] To whom correspondence should be addressed.

0021-9517/93 $5.00

number of earlier investigations, including our own, have shown the utility of temperature programmed reduction/desorption/oxidation studies (*14–17, 26*) and ^{129}Xe NMR experiments (*18, 27–34*) for elucidating metal oxidation state, location, and dispersion, specifically in Pt–NaY zeolite systems. In our previous investigations we reported on physical distributions of platinum species in NaY zeolite and identified chemical species that exist as precursors to reduced Y-zeolite-supported platinum clusters (*18, 26, 31*). In this study, we probe the influence of oxidative processes on the distribution of reduced NaY-supported platinum guests. Raman spectroscopy and ^{129}Xe NMR are employed, in conjunction with hydrogen chemisorption and transmission electron microscopy (TEM), to characterize intracrystalline metal/zeolite structures and compositions and to establish the factors most responsible for metal atom mobility during and after preparatory treatments. In particular, the new application of Raman spectroscopy to this issue provides a direct means of identifying oxide precursors and products to reduced metal species.

METHODS

Pt–NaY samples containing 4.1 wt% or 15 wt% platinum were prepared (*35*) by introducing the tetraammine salt, $Pt(NH_3)_4^{2+}$ (available as $Pt(NH_3)_4Cl_2$ from ICN, Inc.) into commercial Y zeolite (Union Carbide, LZY-52) via the ion-exchange procedure of Gallezot *et al.* (*7*). For the Raman measurements, 0.5 g each of 4.1 wt% and 15 wt% $Pt(NH_3)_4^{2+}$–NaY samples were pelletized under 100 MPa pressure into a 13-mm diameter pellet of 1 mm thickness. Each sample was heated in purified flowing oxygen at a rate of 50 K/h to 673 K, where it was held for 4 h before the Raman spectra were acquired. Raman measurements were made under flowing oxygen using the 488.0 nm line of an argon ion laser (Spectra Physics, Model 165) with 50 mW of power at the sample. A detailed description of the Raman apparatus is found in reference (*36*). Spectra were recorded from 200 cm^{-1} to 1200 cm^{-1}, with a resolution of 6 cm^{-1}. Following completion of the Raman acquisition, the 15 wt% sample was reduced in hydrogen at 298 K, and another Raman spectrum was then acquired. Similarly, Raman spectra were taken on the 15 wt% Pt–NaY sample after each of the following subsequent treatments: reoxidation at 773 K, reduction at 673 K, and reoxidation a second time at 773 K.

For the ^{129}Xe NMR experiments, separate 0.5 g samples of the dried $Pt(NH_3)_4^{2+}$–NaY powder were charged to an upflow reactor, flushed with helium, and calcined individually by heating at 15 K/h to maximum temperatures ranging from 473 K to 873 K in the presence of excess oxygen gas (30 cm^3/s). All feed gases were dried by passage over NaA zeolite dessicant before being directed to the reactor. Upon reaching the upper temperature limit, the furnace was turned off, allowing the insulated reactor to cool to 298 K over a period of many hours. After cooling, the reactor was flushed with helium, after which the samples were reduced separately under identical conditions in purified flowing hydrogen (40 cm^3/s) for 4 h at 673 K. The reduced Pt–NaY catalyst materials were then transferred into 10-mm NMR cells, which were sealed by glass-blowing the loading port shut. After sealing the samples in NMR cells, the reduced Pt–NaY materials were evacuated for 10 h at 673 K to desorb chemisorbed hydrogen and then cooled to ambient temperature. Xenon-129 NMR spectra and adsorption isotherms were obtained on the reduced and degassed Pt–NaY samples (*18, 26*), followed by separate hydrogen chemisorption measurements of accessible surface Pt (*35*). Two reoxidation procedures were employed: the first exposed the reduced, degassed Pt–NaY samples to dry oxygen gas (10 cm^3/s for 6 h) at room temperature, followed by the second which reoxidized the samples at elevated temperatures under the same conditions used in their initial calcinations.

Xenon-129 NMR and adsorption isotherm experiments were performed following each of the reoxidation procedures. The NMR cell was fit with a fritted-glass disk and a high-vacuum stopcock to permit attachment to a vacuum rack for sample degassing and addition of xenon gas for ^{129}Xe NMR and adsorption isotherm experiments. After evacuation of the reoxidized Pt–NaY samples for 10 h at 295 K, xenon gas was introduced to various equilibrium pressures, guided by separate adsorption isotherm experiments (*35*). Xenon-129 NMR spectra of adsorbed xenon were obtained on a Bruker AM-400 spectrometer operating at 110.7 MHz. Typically, 2000 to 20,000 signal acquisitions were accumulated for each spectrum with a recycle delay of 0.2 s between 90° pulses. Chemical shift measurements are precise to within 0.5 ppm and are expressed relative to xenon gas at very low pressure (*28, 37*). Xenon adsorption isotherms were measured for each reoxidized Pt–NaY sample and correlated with the NMR data.

Selected-area bright field TEM images were recorded for reduced and reoxidized Pt–NaY samples to characterize visually sample features larger than about 3 nm. All TEM data were acquired using a JEOL 200CX microscope with a top entry holder and a high resolution pole piece at the National Center for Electron Microscopy at Lawrence Berkeley National Laboratory. Powdered Pt–NaY specimens were suspended in 200 proof ethanol and sonicated for several minutes to break up large aggregates of the micrometer-size zeolite crystallites. A drop of the suspension was placed on a holey carbon film supported on a copper mesh grid, which was subsequently dried in air prior to TEM analysis. The microscope was operated at its maximum accelerating voltage, 200 keV, to minimize electron beam-induced damage of the zeolite (*38, 39*).

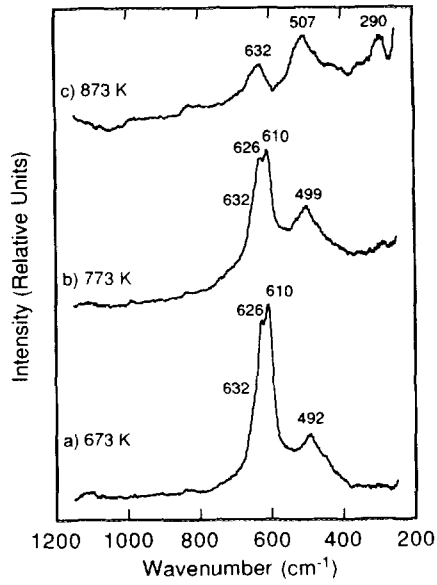

FIG. 1. Raman spectra of 15 wt% $Pt(NH_3)_4^{2+}$–NaY samples calcined in oxygen at (a) 673 K, (b) 773 K, and (c) 873 K.

RESULTS AND DISCUSSION

Preparation of Reduced Pt–NaY

The macroscopic adsorption and reaction properties of metal/zeolite systems depend strongly on the distribution of the reduced metal clusters within or outside the intracrystalline zeolite pore spaces (*1–4*). Physical distribution of the metal is related directly to the chemistry of the metal dispersal process, which frequently involves treatments in oxygen to form platinum oxide (PtO) precursor species. We begin by describing the preparation aspects of reduced Pt–NaY that are important to analysis of the subsequent reoxidation treatments.

Focussing first on the nature of the PtO calcination product, Raman spectroscopy is a sensitive probe of oxide phase, capable of delineating between monomeric, amorphous, and bulk structures through correlation of characteristic molecular vibration frequencies (*36, 40–43*). Raman spectra for 15 wt% $Pt(NH_3)_4^{2+}$–NaY samples calcined in oxygen at different temperatures are shown in Fig. 1. Following calcination at 673 K, which produces essentially complete conversion of $Pt(NH_3)_4^{2+}$ to PtO (Ref. (*26*)), the Raman spectrum of Fig. 1a reveals well-defined peaks at 492, 610, and 626 cm^{-1},

with the latter possessing a shoulder at approximately 632 cm^{-1}. The band at ca. 500 cm^{-1} arises from the Y-zeolite support (*40, 41*), whereas the strong band(s) in the vicinity of 630 cm^{-1} in Fig. 1a reflect the existence of strong metal–oxygen bonds that rule out the formation of Pt^{2+} species bound ionically to the zeolite lattice during calcination at 673 K (*26*). Similar features are present in the sample calcined at 773 K (Fig. 1b), though the sharp peaks at 610 and 626 cm^{-1} are diminished in intensity relative to the zeolite band at 500 cm^{-1}. At 873 K, the sharp peak at 610 cm^{-1} completely disappears, leaving only the bands centered at 507 and 632 cm^{-1} in Fig. 1c. The peak at 630 cm^{-1} is now less intense than the zeolite band at 507 cm^{-1}; the small peak at 290 cm^{-1} is also assignable to the zeolite support (*40, 41*).

The multiple peaks present in the region 610–635 cm^{-1} in Figs. 1a–1c vary in relative intensity, suggesting that multiple PtO species are formed during calcination of $Pt(NH_3)_4^{2+}$–NaY. In particular, the narrow bands at 610 and 626 cm^{-1} observed after calcination at 673 K and 773 K (Figs. 1a and 1b) are absent following similar treatment at 873 K (Fig. 1c). When the peaks at 610 and 626 cm^{-1} are present, however, their relative intensities are constant, indicating that these peaks arise from a single oxide species or phase. This is supported by Raman experiments on calcined Pt–NaY samples containing different metal loadings in which the relative proportions of different species or phases present are expected to be different. As shown in Fig. 2, Raman spectra for 4.1 wt% and 15 wt% Pt–NaY calcined at 673 K display peaks at 610 and 626 cm^{-1} with identical relative intensities. These peaks are attributed to small crystallites of PtO that possess more homogeneous Pt–O scattering environments, and therefore narrower Raman lines, than dispersed PtO species. The two lines apparently arise from a PtO phase that adopts a structure with reduced symmetry inside the NaY supercages. The

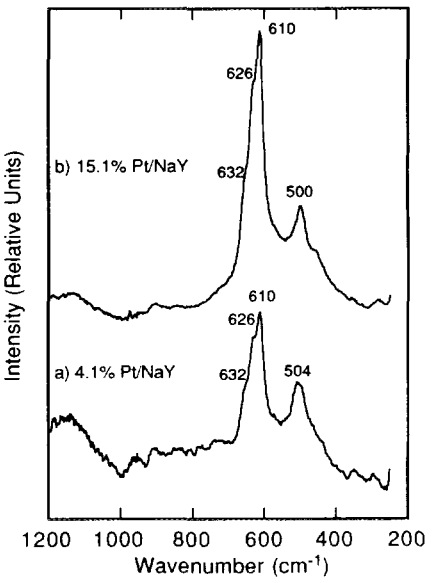

FIG. 2. Raman spectra of (a) 4.1 wt% and (b) 15 wt% $Pt(NH_3)_4^{2+}$–NaY samples calcined in oxygen at 673 K.

broader band centered at 632 cm^{-1} is probably due to highly dispersed or amorphous PtO species, which are expected to have a wider distribution of Pt–O bond lengths (*42*). These interpretations are consistent with recent Raman experiments by Graham *et al.* (*43*) on crystalline phases of PtO_x, including PtO, PtO_2 (α and β phases), Pt_3O_4, and Pt_5O_6.

Based on the insight provided by the Raman experiments, and retaining consistency with observed product evolution in earlier temperature programmed desorption/oxidation work (*10, 11, 14, 15*), the relevant calcination reactions at 673 K are

$$Pt(NH_3)_4^{2+}\text{–}2Y + \tfrac{3}{2}O_2 \rightarrow PtO + 2\,NH_4^+\text{–}Y + N_2 + 2\,H_2O \quad (1)$$

$$\tfrac{3}{2}O_2 + 2\,NH_4^+\text{–}Y \rightarrow 2\,H^+\text{–}Y + N_2 + 3\,H_2O. \quad (2)$$

We cannot exclude the possibility of autoreduction occurring as a step to the formation of PtO in Eq. (1) above, though it seems unnecessary to invoke such a reduction/reoxidation path,

$$Pt(NH_3)_4^{2+}\text{–}2Y + \tfrac{5}{2}\,O_2 \rightarrow Pt^{(0)} + 2\,H^+\text{–}Y + 2\,N_2 + 5\,H_2O \quad (3)$$

$$Pt^{(0)} + \tfrac{1}{2}\,O_2 \rightarrow PtO, \quad (4)$$

because the Pt species can apparently remain in the (II) oxidation state throughout the calcination process. If autoreduction occurs (Eqs. (3) and (4)), the lifetime of any $Pt^{(0)}$ precursor (if it indeed exists) must be sufficiently short at 673 K to inhibit migration and agglomeration of neutral metal species. The identification of supercage PtO as the preferred product of calcination differs from other studies (*7, 14–17*), which have considered supercage Pt^{2+} cations to be the desirable precursor to highly dispersed $Pt^{(0)}$. At higher calcination temperatures (773–873 K), the metal oxide species can react with nearby acid sites, producing divalent metal cations and H_2O according to the reaction (*26*)

$$PtO + 2\,H^+\text{–}Y \rightarrow Pt^{2+}\text{–}2Y + H_2O, \quad (5)$$

whereupon the Pt^{2+} cations migrate to lower energy sites in the sodalite cages (*7, 14–17, 26*).

After reduction of calcined Pt–NaY samples at 673 K, the fraction of surface platinum metal present, shown in Table 1, depends on the temperature of the preparatory calcination treatments. The nominal adsorption stoichiometry of 1 H/1 Pt permits the amount of accessible surface metal present in reduced Pt–NaY samples to be estimated from hydrogen uptake measurements (35, 44–46). Since the 0.29-nm kinetic diameter of the hydrogen molecule exceeds the 0.22-nm opening of the Y-zeolite sodalite cage at room temperature, the fraction of surface platinum reported in Table 1 reflects only that in exterior or supercage locations, where the metal is accessible to diffusing hydrogen (and also to xenon.) Neglecting the contribution from large low-surface-area clusters on the periphery of the crystallites, the dispersion measured using H_2-chemisorption at room temperature corresponds essentially to reduced Pt clusters (>1 atom) in the supercages.

TABLE 1

Accessible Surface Platinum in Reduced Pt–NaY Samples (Top) Calcined at Different Temperatures and (Bottom) for the Same Samples, Following Reoxidation at the Temperatures Shown

Sample	Calcination (K)	Reduction (K)	Fraction of surface Pt
a	473	673	0.06
b	573	673	0.61
c	673	673	0.74
d	773	673	0.42
e	873	673	0.15
Sample	**Reoxidation (K)**	**Reduction (K)**	**Fraction of surface Pt**
c′	673	673	0.76
d′	773	673	0.43
e′	873	673	0.15

Note. Surface Pt was determined from hydrogen chemisorption at 293 K (*45*).

For the Pt–NaY sample calcined at 473 K and reduced at 673 K, the TEM micrograph shown in Fig. 3 reveals very large platinum clusters (ca. 40 nm) on the exterior of the micrometer-size zeolite crystallite that account for the low (6%) metal dispersion in Table 1, sample a. Most of the platinum present in this sample is in the form of very large agglomerates. A single 1-μm diameter Pt–NaY crystallite, for example, contains enough metal to produce about 20 clusters 40 nm in diameter (3×10^6 Pt atoms/cluster). This is consistent with the approximate number of such large clusters present on the exterior surface of the sample depicted in Fig. 3 (see also Fig. 16 to follow.) Accordingly, xenon adsorbed in predominantly empty NaY cavities in the crystallites' interior accounts for the comparatively low ^{129}Xe chemical shift values observed in Fig. 4 (for the reduced sample with large external Pt aggregates), compared to samples containing reduced, highly dispersed Pt (e.g., Fig. 7).

For the Pt–NaY samples calcined at 573 and 673 K, more complete conversion of

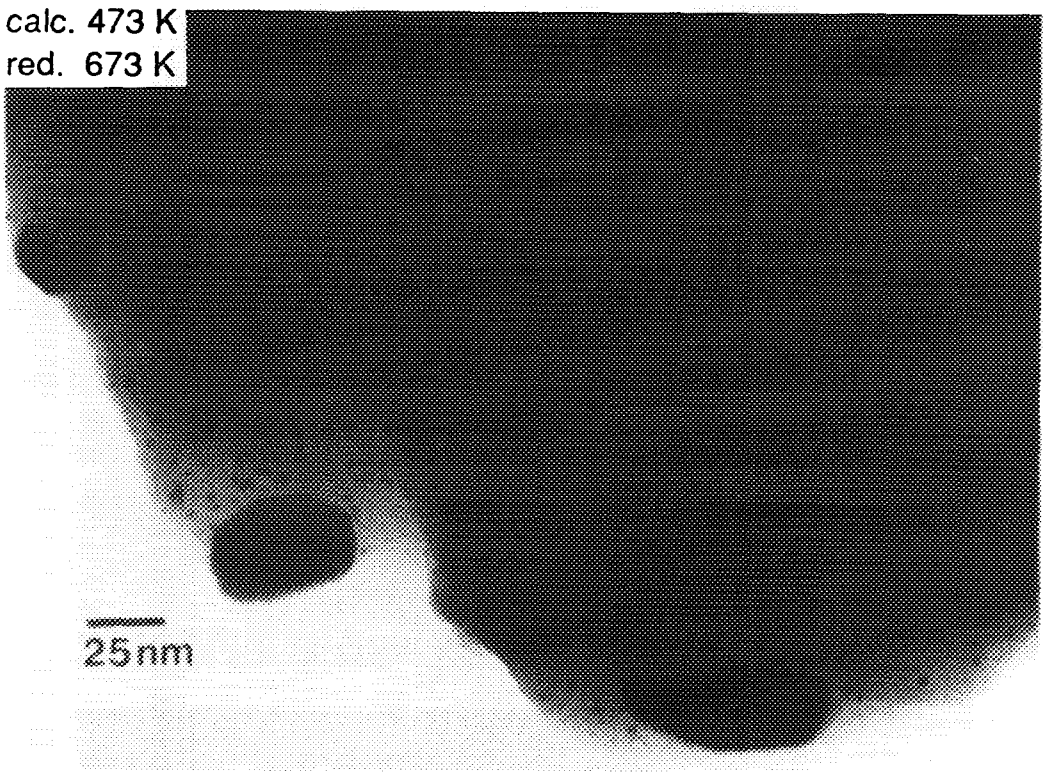

FIG. 3. Transmission electron micrograph of reduced 15 wt% Pt–NaY after calcination of the Pt $(NH_3)_4^{2+}$-exchanged zeolite at 473 K and then reduction of the calcined catalyst at 673 K.

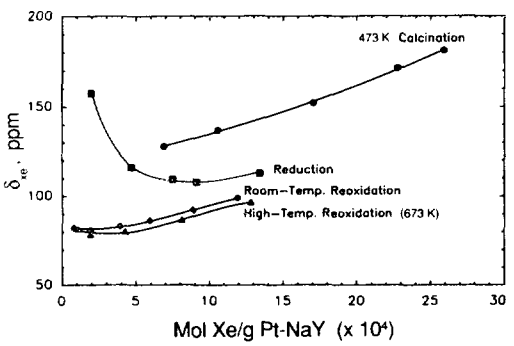

FIG. 4. Variation in ^{129}Xe chemical shift with the concentration of xenon adsorbed (T = 295 K) on 15 wt% Pt–NaY after each of the following treatments: initial calcination at 473 K, reduction at 673 K, chemisorption of oxygen at 295 K, and reoxidation at 673 K.

$Pt(NH_3)_4^{2+}$ to PtO occurs (Eqs. (1) and (2)), providing more of the platinum oxide precursor species preferred for the formation of highly dispersed metal within the supercages upon reduction (*26*). This is manifested by higher fractions of exposed platinum atoms (Table 1, b, c), by the absence of large aggregates on the crystallite surface (Figs. 5a and 5b), and by larger ^{129}Xe chemical shifts in the reduced samples as shown in Figs. 6 and 7 (*18*).

For the reduced Pt–NaY samples calcined at 773 K and 873 K, penetration of the metal species (as Pt^{2+}, Eq. (5)) into the sodalite cages during the high temperature calcination treatments (*7, 14–17, 26, 32*) results in lower fractions of accessible Pt (Table 1, d, e). In addition, smaller ^{129}Xe chemical shifts are observed (Figs. 8 and 9)

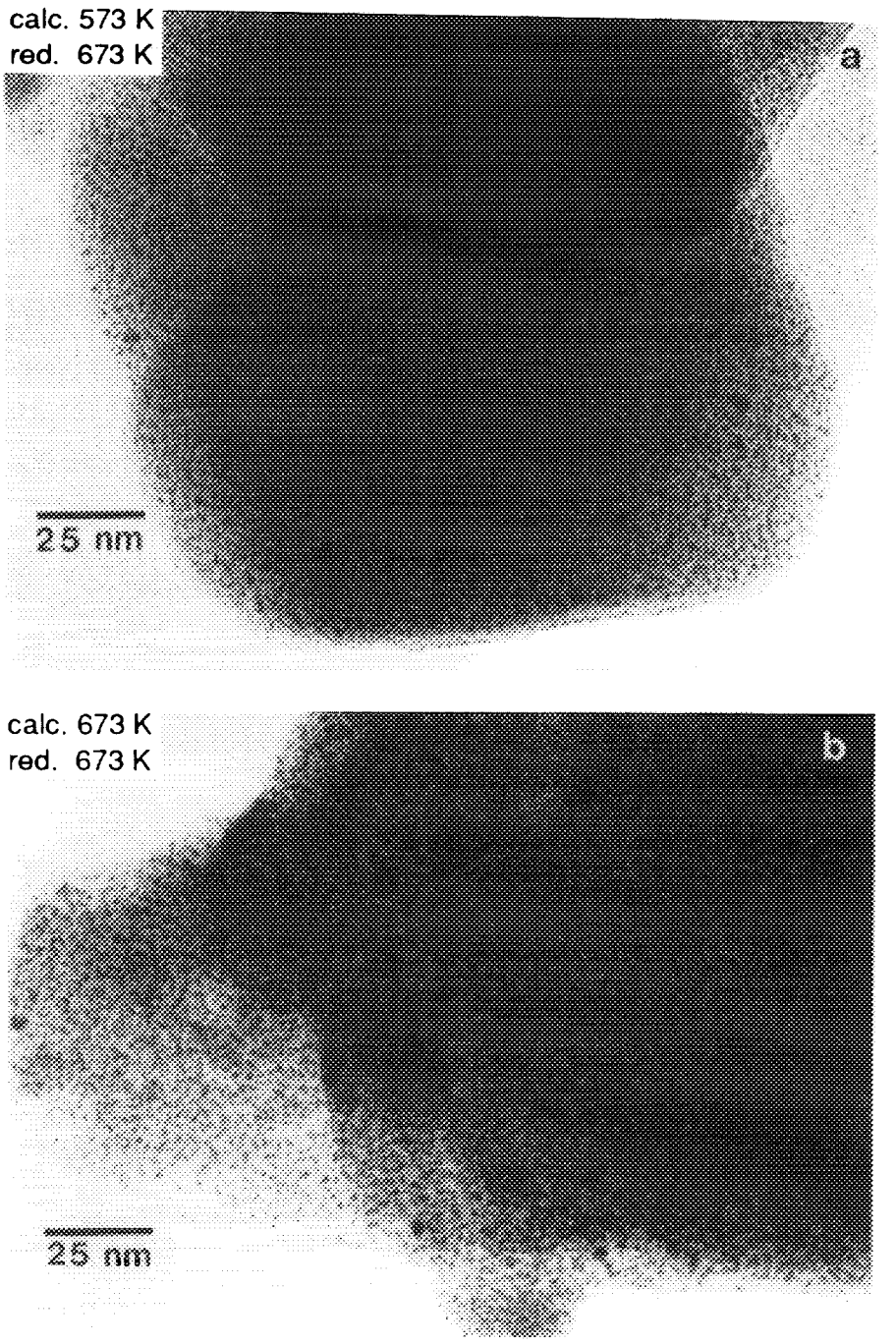

FIG. 5. Transmission electron micrographs of reduced 15 wt% Pt-NaY (a) following calcination of the $Pt(NH_3)_4^{2+}$-exchanged zeolite at 573 K and subsequent reduction of the calcined catalyst at 673 K and (b) following calcination of the $Pt(NH_3)_4^{2+}$-exchanged zeolite at 673 K and subsequent reduction of the calcined catalyst at 673 K.

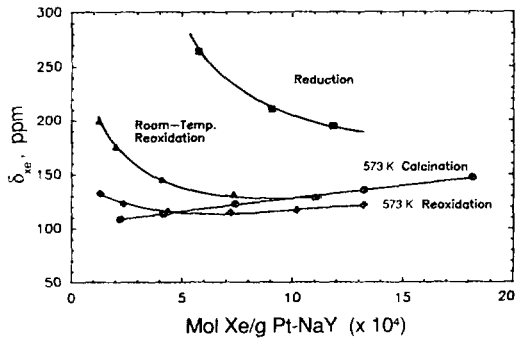

FIG. 6. Variation in ^{129}Xe chemical shift with the concentration of xenon adsorbed (T = 295 K) on 15 wt% Pt–NaY after each of the following treatments: initial calcination at 573 K, reduction at 673 K, chemisorption of oxygen at 295 K, and reoxidation at 573 K.

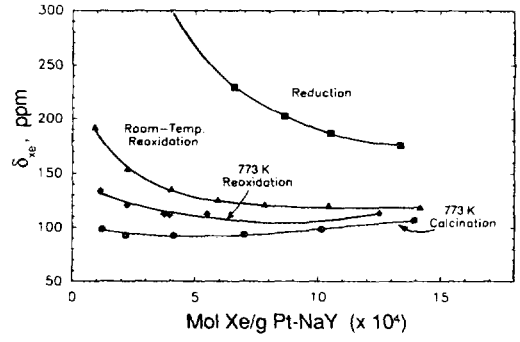

FIG. 8. Variation in ^{129}Xe chemical shift with the concentration of xenon adsorbed (T = 295 K) on 15 wt% Pt–NaY after each of the following treatments: initial calcination at 773 K, reduction at 673 K, chemisorption of oxygen at 295 K, and reoxidation at 773 K.

compared to the reduced sample calcined at 673 K (Fig. 7), where nearly all Pt is highly dispersed in the supercages. Temperature programmed reduction data for the samples calcined at 773 K and 873 K indicate that only about two-thirds of the platinum species in the sodalite cavities are reduced at 673 K in hydrogen (*26, 35*). During reduction, some of the metal migrates as neutral atoms from sodalite cage sites back into supercage environments (*7, 14–16*), where it is accessible to both hydrogen and xenon, though a significant fraction remains in the sodalite cages as $Pt^{(0)}$ or Pt^{2+}. Following reduction of our samples, enhanced ^{129}Xe chemical shift values (Figs. 8 and 9) compared to the respective calcined-only materials (where most Pt is in the sodalite cages as Pt^{2+}) and the nonzero fractions of surface Pt (Table 1, d, e) suggest that the reaction of hydrogen with Pt^{2+} in the sodalite cavities produces a migratory intermediate that tends to agglomerate as reduced metal in the supercages. Aggregation of platinum in supercage sites under these circumstances is supported by the TEM micrographs shown in Figures 10a and 10b, which reveal numerous reduced metal clusters larger than

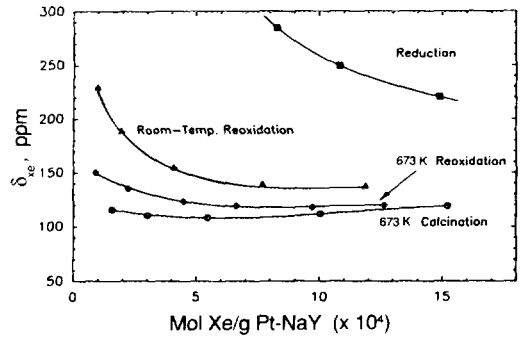

FIG. 7. Variation in ^{129}Xe chemical shift with the concentration of xenon adsorbed (T = 295 K) on 15 wt% Pt–NaY after each of the following treatments: initial calcination at 673 K, reduction at 673 K, chemisorption of oxygen at 295 K, and reoxidation at 673 K.

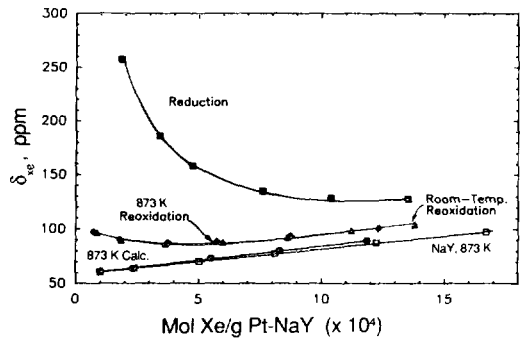

FIG. 9. Variation in ^{129}Xe chemical shift with the concentration of xenon adsorbed (T = 295 K) on 15 wt% Pt–NaY after each of the following treatments: initial calcination at 873 K, reduction at 673 K, chemisorption of oxygen at 295 K, and reoxidation at 873 K.

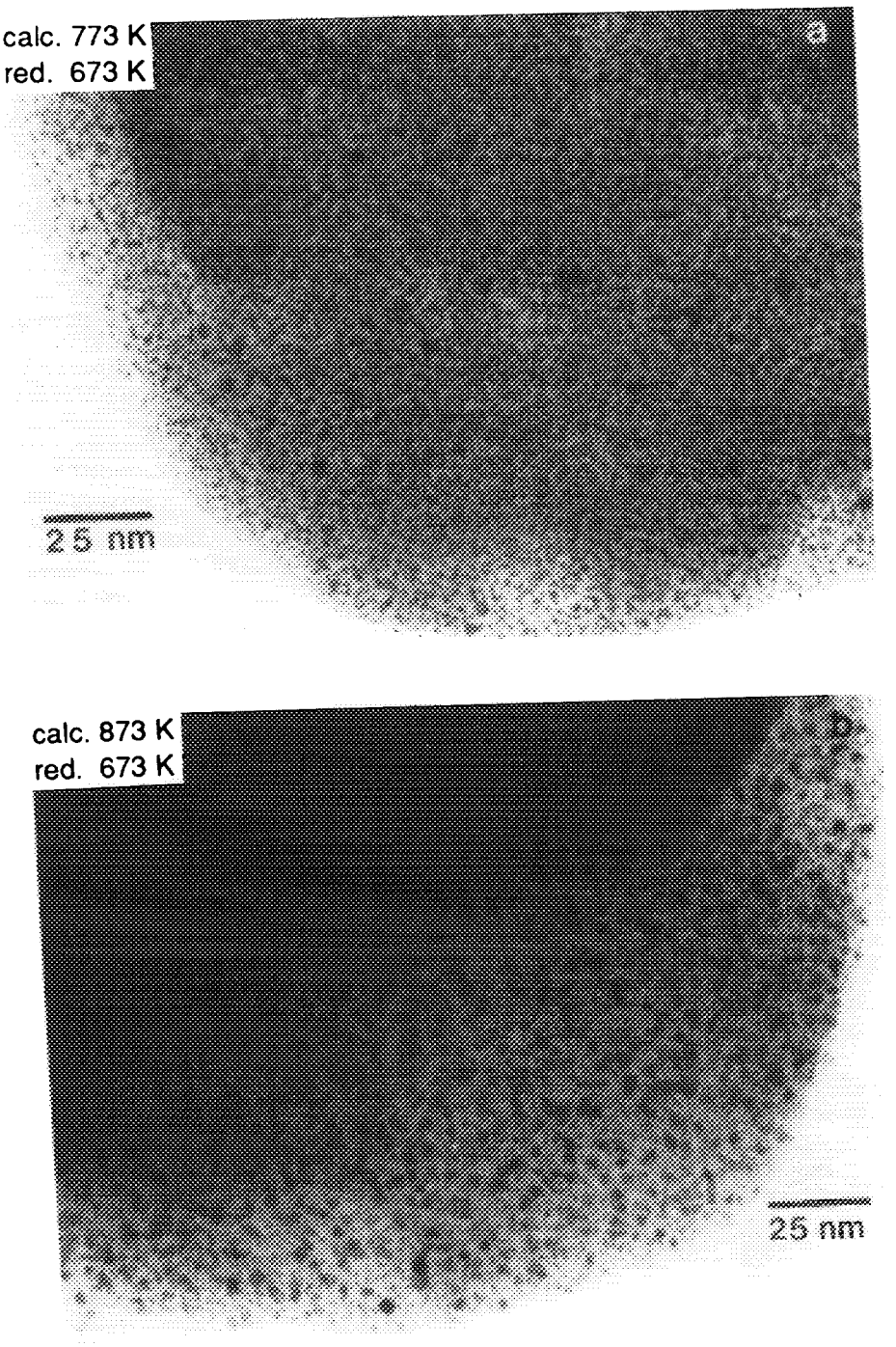

FIG. 10. Transmission electron micrographs of reduced 15 wt% Pt–NaY (a) following calcination of the $Pt(NH_3)_4^{2+}$-exchanged zeolite at 773 K and subsequent reduction of the calcined catalyst at 673 K and (b) following calcination of the $Pt(NH_3)_4^{2+}$-exchanged zeolite at 873 K and subsequent reduction of the calcined catalyst at 673 K.

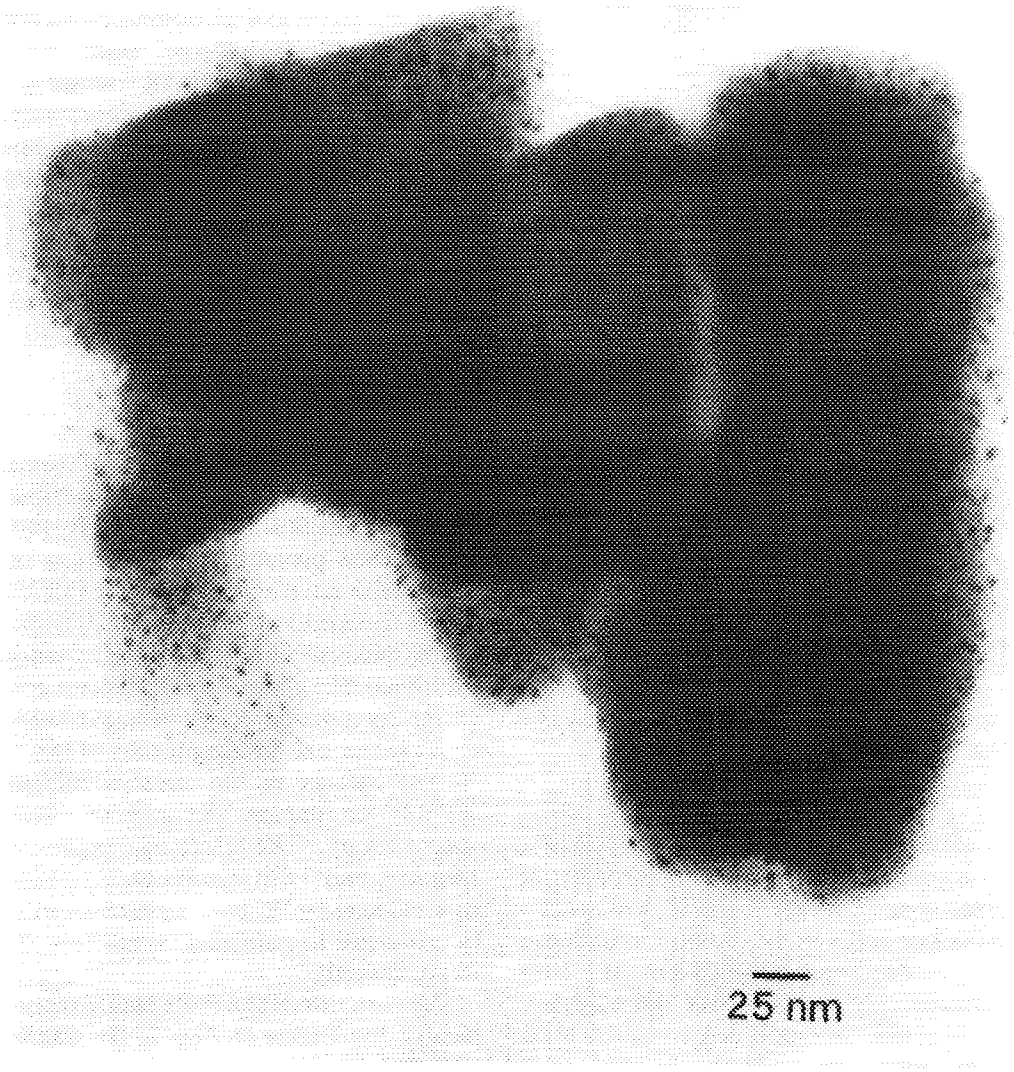

FIG. 11. Transmission electron micrograph of reduced 15 wt% Pt–NaY following calcination at 873 K and subsequent reduction at 673 K. The particle shown is from the same sample depicted in Figure 10b but at lower magnification.

the 3-nm resolution limit of the brightfield imaging technique. In the projected images provided by the TEM experiments, the contribution from metal clusters situated on the exterior zeolite surface to the observed cluster density is essentially independent of zeolite particle thickness. In Fig. 11, however, no (or few) clusters are observed on the crystallite's periphery. Furthermore, the density of Pt clusters is greater in zones of greater crystallite thickness. This points to the occlusion of large Pt clusters within the zeolite matrix (*47, 48*) during reduction at 673 K, rather than migration of Pt atoms (0.27 nm diameter) from sodalite sites to the exterior crystallite surface before agglomeration (*16*).

Local structural damage, which may result from the growth of large metal clusters in the NaY supercages, may not affect the

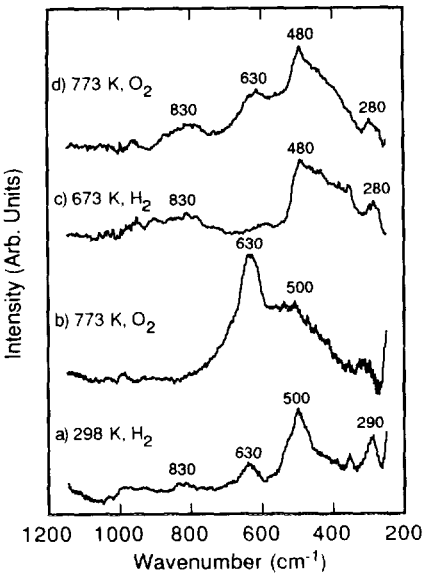

FIG. 12. Raman spectra of 15 wt% $Pt(NH_3)_4^{2+}$-NaY samples after calcination at 673 K, followed by various (sequential) reduction or reoxidation treatments: (a) reduction in hydrogen at 298 K; (b) reoxidation at 773 K; (c) reduction in hydrogen at 673 K; and (d) reoxidation at 773 K.

overall crystallinity of the framework (*47*). These observations are corroborated by the Raman spectra in Figs. 2 and 12, which show only minor shifts in the phonon frequencies of the zeolite support. Occlusion of a 3-nm Pt cluster in 15 wt% Pt–NaY, for example, may produce structural defects in a few adjacent supercages (perhaps 2%), while most in the immediate vicinity remain intact. Since enough metal exists in the 15 wt% Pt–NaY system to produce 3×10^5 Pt clusters 3 nm in diameter (1300 Pt atoms/cluster) within each micrometer-size crystallite, most of the Pt is in the form of either small reduced metal clusters below the 3-nm TEM resolution limit or unreduced Pt^{2+} cations in the sodalite cages. Clearly from Fig. 11, the number of Pt clusters observed in the 3-nm size range is significantly less than the maximum number possible. For the reduced Pt–NaY samples calcined at 773 K and 873 K, the relatively low ^{129}Xe chemical shift measurements in Figs. 8 and 9 (compared to Fig. 7) and the low hydrogen uptake manifested in Table 1e indicate, moreover, the lack of an appreciable quantity of highly dispersed Pt in the supercages accompanying the large clusters. From this it is apparent that Pt present in the supercages is predominantly in the form of large clusters (corroborated by reoxidation experiments discussed below), though most of the metal remains in sodalite sites as one- or two-atom reduced species or as divalent platinum cations.

Pt/NaY Reoxidation

The structure and stability of reduced metal clusters are known to be functions of aggregate size (*49–57*). This directly affects the reaction properties of dispersed platinum, which have been shown to exhibit particle-size dependent behavior (*2, 7, 9, 20, 23, 30, 58–60*). An important issue is whether additional migration of the Pt species occurs during reoxidation of the reduced metal to increase the size and/or number of the large clusters or, as in the case of palladium (*61–63*), to induce redispersion. Raman spectroscopy, ^{129}Xe NMR, hydrogen chemisorption, and TEM can be used to investigate changes in Pt–NaY systems produced by exposure to oxidizing conditions of differing severity.

The structure of the PtO species responsible for the bands in Fig. 1, for example, is corroborated by Raman experiments that probe reduction and reoxidation effects in these materials. Figure 12a shows the Raman spectrum of 15 wt% Pt–NaY initially calcined at 673 K and subsequently reduced in hydrogen at 298 K. Zeolite bands near 290 and 500 cm^{-1} are present, along with a small broad feature at 630 cm^{-1} arising from a small amount of unreduced (probably subsurface) PtO. Comparison with the Raman spectrum in Fig. 1a from the initially calcined sample reveals that the narrow peaks at 610 and 626 cm^{-1} have disppeared. Subsequent reoxidation of this sample at 773 K shows a marked increase in the intensity of the 630 cm^{-1} peak relative to the NaY band

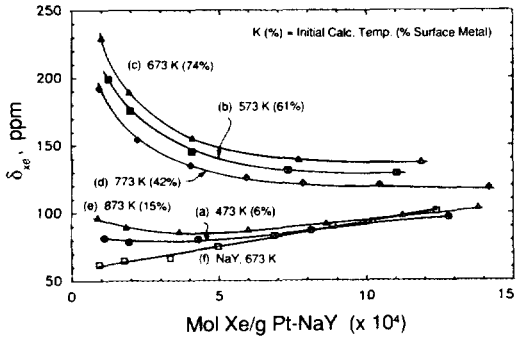

FIG. 13. Variation in ^{129}Xe chemical shift with the concentration of xenon adsorbed (T = 295 K) on 15 wt% Pt–NaY zeolite samples reoxidized by exposure of the reduced catalysts to oxygen gas at room temperature. The metal–zeolite samples were previously reduced at 673 K after calcination at different temperatures: (a) 473 K, (b) 573 K, (c) 673 K, (d) 773 K, (e) 873 K, (f) NaY dehydrated at 673 K. The percentage of surface Pt in the supercages (prior to reoxidation) is shown in parentheses for each sample.

at 500 cm^{-1} in Fig. 12b. The absence of narrow peaks at 610 and 626 cm^{-1} in the reoxidized material indicates that no small PtO crystallites are present. Following more severe reduction conditions at 673 K (Fig. 12c), the band at 630 cm^{-1} also disappears, leaving only bands at 280 and 480 cm^{-1} from the zeolite lattice and a broad feature at 829 cm^{-1} that is attributed to the quartz cell. Reoxidation of the same sample again at 773 K restores the peak at 630 cm^{-1} in Fig. 12d, though it is less intense than apparently the same band in Fig. 12b produced by reoxidation at 773 K following reduction at room temperature. The decrease in PtO signal intensity likely arises from a broader distribution of surface environments created during the reduction treatment at 673 K. The observed reduction/reoxidation behavior is consistent with our assignment of the broad feature at 630 cm^{-1} to dispersed or adsorbed Pt–O species and the narrow bands at 610 and 626 cm^{-1} to microcrystalline PtO, which is not expected to be regenerated because of oxygen mass transport limitations discussed below.

Figures 13 and 14 display ^{129}Xe chemical shift data for xenon adsorbed on Pt–NaY systems following reoxidation at ambient and high temperature, respectively. The reoxidation treatments were performed on previously calcined and reduced Pt–NaY samples as described above. Compared with ^{129}Xe NMR data for the reduced, outgassed Pt–NaY sample (Fig. 7), Figure 13 shows that ^{129}Xe chemical shifts are substantially lower for a given xenon uptake following reoxidation of the catalyst at room temperature. Chemisorption of gases onto reduced Pt clusters at room temperature partially shields the ^{129}Xe probe atoms from the conduction electrons of the metal cluster, reducing the heat of xenon adsorption (compared to Xe adsorbed on the reduced metal) and diminishing the ^{129}Xe shift (*18, 27–30*). The relative magnitudes of the ^{129}Xe shifts correlate with the amount of Pt accessible to the xenon probe species, generally corresponding to that in the supercages. No migration of the metal is expected or observed during chemisorption of O_2 at 295 K (*7, 45*).

Reoxidation of the Pt–NaY samples at elevated temperatures, however, affects the materials differently. In the samples possessing a preponderance of small clusters

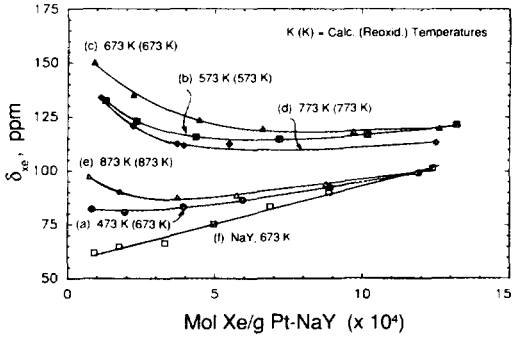

FIG. 14. Variation in ^{129}Xe chemical shift with the concentration of xenon adsorbed (T = 295 K) on 15 wt% Pt/NaY zeolite samples reoxidized at the temperatures of the catalysts' initial calcination (with the exception of sample (a) which was reoxidized at 673 K. The metal–zeolite samples were previously reduced at 673 K after calcination at different temperatures: (a) 473 K, (b) 573 K, (c) 673 K, (d) 773 K, (e) 873 K, (f) NaY dehydrated at 673 K.

(namely those calcined at 573 K, 673 K, or 773 K), the ^{129}Xe chemical shifts are significantly smaller (Figs. 14b–14d) after high-temperature reoxidation compared to the shifts measured in the same samples chemisorbed with oxygen at room temperature (Figs. 13b–13d). Such is not the case for samples possessing a large fraction of large clusters in exterior and/or supercage sites accessible to both oxygen (0.28 nm kinetic diameter) and xenon, for which little or no additional shielding of the Pt species is observed after oxidation at elevated temperatures. Comparing Figs. 13a and 13e with Figs. 14a and 14e, for example, reveals very little change in the ^{129}Xe chemical shift data for large cluster systems following high-temperature reoxidation of reduced samples initially calcined at 473 K and 873 K. These observations are more clearly seen in Figs. 4 and 6–9, where ^{129}Xe chemical shift data are presented as a function of treatment history for each Pt–NaY sample.

The cluster-size-dependent response of the materials to reoxidation at elevated temperatures can be understood in terms of the relative reactivities of the small and large metal particles. Small clusters of metal atoms are, in general, more reactive than large aggregates due to lower activation energy barriers to structural rearrangements (*57, 64, 65*). As shown schematically in Figs. 15a and 15b, small metal clusters may be more readily oxidized than large particles (*52*), leading to more complete oxidation of highly dispersed metal at elevated temperatures. As more of the conduction electrons of the metal become localized in covalent Pt–O bonds, Xe probe atoms near the metal species become more effectively shielded. A thicker passivation layer of adsorbed oxygen apparently diminishes the perturbing influence of reduced Pt in the core of the cluster on the highly mobile, physisorbed ^{129}Xe atoms. This would account for the lower ^{129}Xe shifts observed in Figs. 14b–14d associated with Pt–NaY samples reoxidized at high temperature, compared to ^{129}Xe shifts shown in Figs. 13b–13d for Pt–NaY systems reoxidized at room temperature.

For larger metal particles, hindered oxygen transport to reduced metal in the center of the clusters apparently prevents the oxidation process from proceeding to completion (during the 5–10 h reoxidation times employed in this study.) Formation of a thin oxide layer at a metal interface has been observed to passivate large clusters leading to incomplete oxidation of the metal (*66*). As depicted in Fig. 15b, a diffusion-limited oxidation process at the relatively low temperatures employed here results in a substantial portion of the metal remaining in the reduced state beneath a thin layer of PtO on the cluster periphery. Little additional shielding is expected between the metal guest and the ^{129}Xe probe species under these circumstances. This is consistent with experimental observations in Figs. 4, 9, 13a, 13e, 14a, and 14e, which reveal that the ^{129}Xe shifts measured after the ambient and high-temperature reoxidation treatments are nearly identical for systems with a preponderance of clusters larger than 3 nm.

The stability of zeolite-supported metal clusters to cyclic oxidation and reduction is studied using hydrogen chemisorption and TEM. In Table 1, c′–e′, for example, the fraction of surface platinum metal present nominally in the NaY supercages is unchanged (within +3% experimental error) in Pt–NaY samples reoxidized at the temperatures used in the materials' initial calcination (compare with Table 1, c–e). This indicates that after initial calcination at 673–873 K and reduction at 673 K, reduced and ionic platinum species remain stably bound in supercage or sodalite sites both during treatment in oxygen at elevated temperatures and during multiple reductions at 673 K. After numerous reductions of samples initially calcined at 773 K and 873 K, the nonmigratory character of unreduced Pt^{2+} species remaining in the sodalite cages is consistent with a severely mass-transport-limited reduction process at 673 K. Sodalite-confined Pt^{2+} cations are readily reduced, providing the reducing agent(s), in this case H_2 or zeolite protons, can surmount the po-

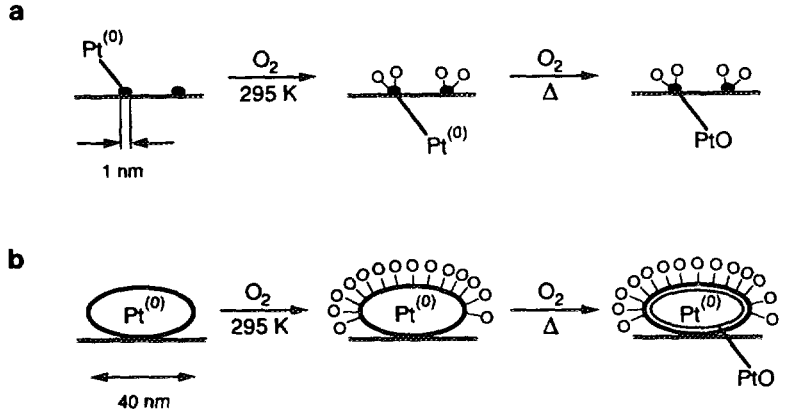

FIG. 15. Schematic diagram depicting the effect of cluster size on platinum oxidation under different thermal conditions (a) 1-nm Pt particles and (b) 40-nm Pt particles. The diameters of the reduced clusters reflect the approximate particle sizes obtained following reduction of Pt-NaY samples initially calcined at 673 K and 473 K, respectively.

tential barrier to penetrate the sodalite apertures. The potential barrier to penetration apparently has a steep temperature dependence, so that over many hours at 673 K no furtherance of the reduction reaction is observed.

In addition, hydrogen chemisorption experiments demonstrate that reoxidation of Pt–NaY systems at temperatures equivalent to the initial calcination temperature up to 873 K does not alter the surface area of the metal in the Y zeolite supercages (Table 1, samples d, d'; e, e'). TEM micrographs of very large cluster Pt–NaY systems, such as those shown in Fig. 16, indicate that reoxidation at 673 K also has little effect on the size or number of large metal particles present. Though loss of metal crystallinity has been reported for large Pt particles supported on SiO_2 or γ-Al_2O_3 during reoxidation at elevated temperatures (*67*), this is not apparent in Fig. 16. The metal clusters visible in Fig. 16b reveal little deterioration in the crystallinity of Y-zeolite-supported Pt as a result of reoxidation at 673 K. No additional migration of the metal species apparently occurs as result of the high temperature oxygen–hydrogen titration processes employed in this study. This differs from high-temperature reoxidation of palladium–NaY, where reduced $Pd^{(0)}$ aggregates have been observed to undergo redispersion under similar conditions (*61–63*).

Low Metal Loadings

Since ^{129}Xe NMR relies on changes in chemical shift to reflect changes in metal–guest chemistry or distribution, the technique requires a sufficient concentration of the metal species to produce measurably different ^{129}Xe shifts in samples subjected to different preparatory treatments. The sensitivity of the ^{129}Xe probe to highly dispersed, reduced metal permits lower, more industrially realistic metal loadings to be studied. Figure 17, for example, shows the effect of diminished platinum loadings on the ^{129}Xe chemical shift in Pt–NaY, calcined and subsequently reduced at 673 K, as a function of the concentration of adsorbed xenon. This is consistent with earlier ^{129}Xe shift versus pressure data of Petrakis *et al.* (*32*). Loadings down to 0.5 wt% Pt produce discernible shifts in the ^{129}Xe resonance at low adsorbed xenon concentrations. Unfortunately, low sensitivity of the ^{129}Xe shift to shielded metal species, such as PtO, is troublesome at low metal guest loadings. In these cases, use of 80% enriched ^{129}Xe or

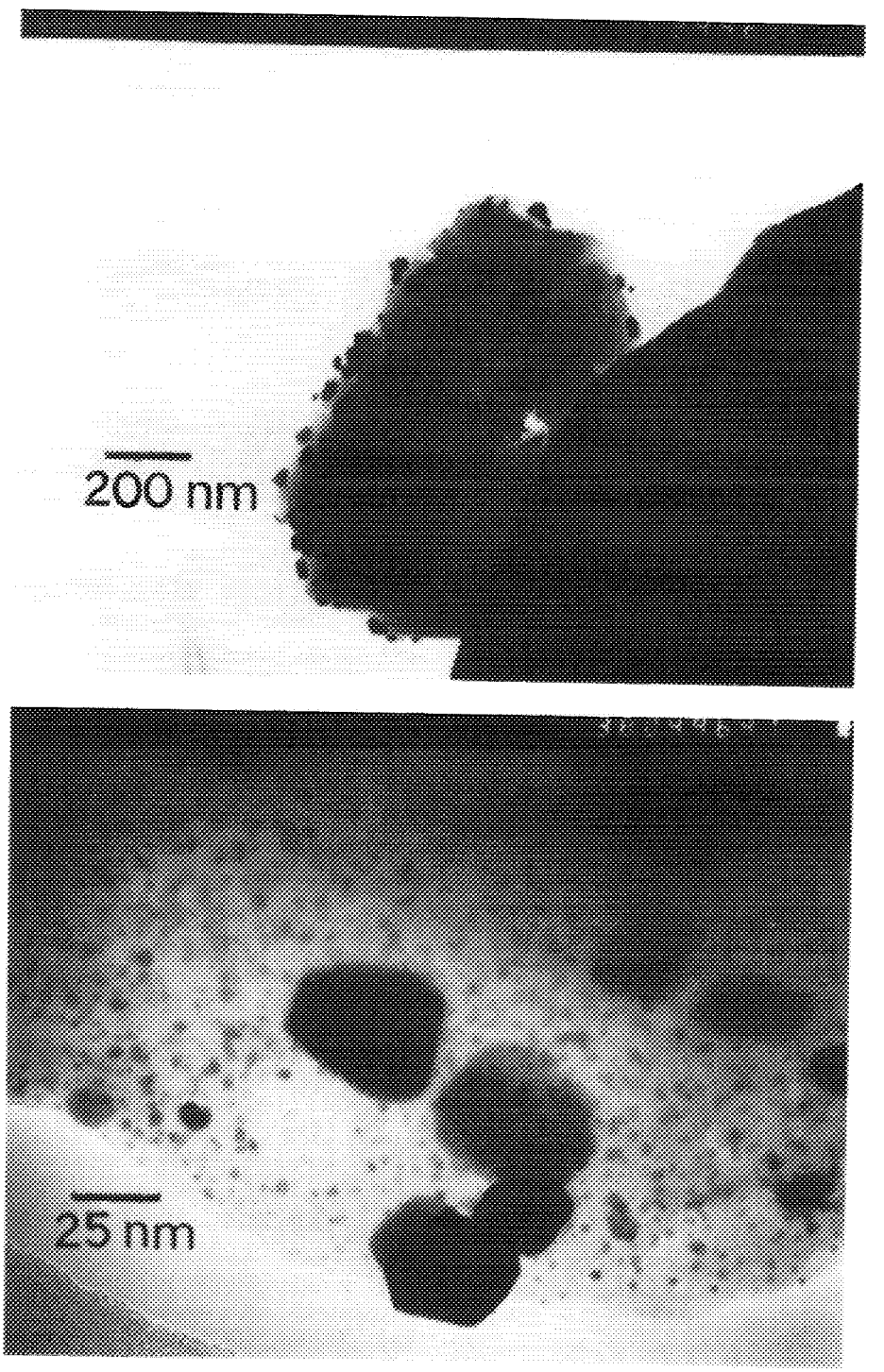

FIG. 16. Transmission electron micrographs of 15 wt% Pt–NaY containing very large clusters following reoxidation of the catalyst at 673 K. The sample was initially calcined at 473 K and reduced at 673 K prior to the reoxidation treatment. (a) Low magnification view (×52,000) showing ca. 40-nm Pt clusters on the exterior surface of a single crystallite. The dark feature on the right is a portion of the Cu grid. (b) High magnification view (×380,000) showing the crystallinity of some of the larger Pt clusters.

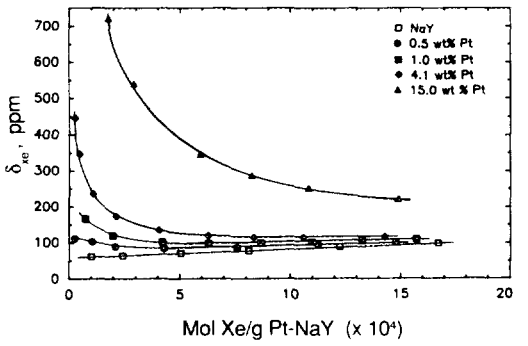

FIG. 17. Variation in ^{129}Xe chemical shift with the concentration of xenon adsorbed (T = 295 K) on reduced Pt–NaY zeolite samples containing variable metal loadings. After initial ion-exchange treatments, the samples were handled identically, including calcination at 673 K and subsequent reduction at 673 K. Variations in metal dispersion among the samples (55–74%), measured using H_2 chemisorption, exert some influence on the value of the observed shifts, though the dominant effect is due to the concentration of metal present in the samples.

adoption of new optically pumped ^{129}Xe NMR methods (*68, 69*) may enhance the technique's sensitivity to the metal species by permitting studies at low Xe uptakes where Xe–metal interactions predominate.

CONCLUSIONS

Characterization of reduced and reoxidized Pt–NaY complements our earlier experimental investigations that provide corroborative data on the identities and locations of precursor species to reduced Pt clusters in NaY zeolite (*18, 26*). The present study, in conjunction with this previous work, permits unambiguous description of the chemistry governing platinum dispersal in NaY zeolite for the specific set of conditions employed here. For the slow thermal ramp rates and high reactant gas flows used, these results establish that calcination at 673 K (with subsequent reduction at 673 K) provides near-optimal conditions for dispersal of reduced platinum in 15 wt% Pt–NaY, with PtO being the desired precursor for maximizing metal surface area in the reduced material. The identification of PtO as a precursor to highly dispersed reduced $Pt^{(0)}$ located in NaY supercages differs from earlier investigations of this system prepared under similar conditions. Though much of the underlying chemistry is expected to be broadly applicable, care should be exercised in generalizing these results to other treatment conditions for dispersal of platinum (or other metals) into intracrystalline zeolite channels, particularly in the presence of other cations, metal ligands, or when different loading procedures are employed (*4, 19, 20*).

Figure 18 summarizes the preparation chemistry (and the resulting metal distributions) for the various calcination treatments used in this study for dispersing platinum species within 15 wt% Pt–NaY. Treatment in oxygen at 473 K generally dehydrates the $Pt(NH_3)_4^{2+}$-exchanged zeolite, without widespread reaction of the tetraammine species, while coulombic interactions with the lattice keep the divalent complexes tethered to anion sites within the supercages. For Pt–NaY incompletely calcined at 473 K, reduction of platinum to the metallic state at 673 K induces migration of the metal species to the exterior of the crystallites, where subsequent aggregation of the platinum can produce large, catalytically undesirable clusters. During calcination at 673 K, the platinum tetraammine complex reacts with oxygen to form essentially nonmigratory PtO that remains in supercage locations, where in hydrogen at 673 K, it can be readily reduced. For the conditions examined, calcination at 673 K and subsequent reduction at 673 K produces reduced platinum metal with the highest accessible surface area in supercage locations. Calcination at temperatures from 773 K to 873 K converts $Pt(NH_3)_4^{2+}$ to PtO, which subsequently reacts further with framework acid sites to produce Pt^{2+} cations. Migration of the divalent platinum cations into sodalite cages following these high-temperature calcination treatments renders reduction of the platinum guests more difficult and, in fact, incomplete at 673 K.

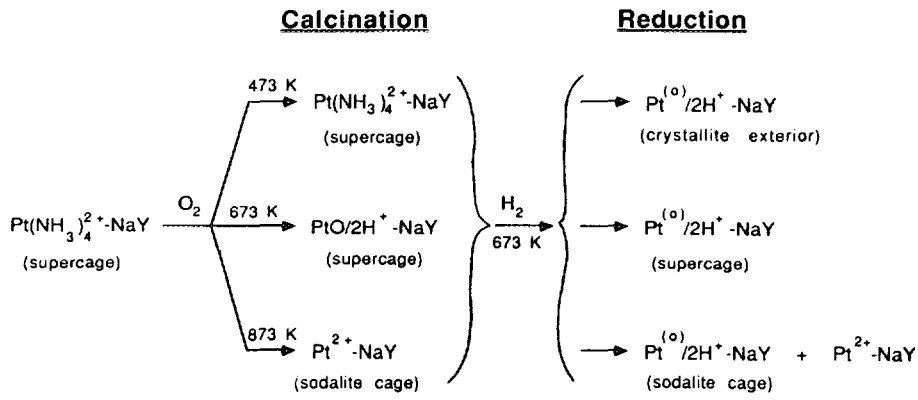

FIG. 18. Summary of Pt–NaY preparation chemistry for different calcination conditions. Primary locations of the metal species are indicated in parentheses.

After initial reduction of Pt–NaY, subsequent reoxidation up to 873 K does not induce or abet additional agglomeration of the metal species into larger clusters. The cluster-size-dependent response of the Pt–NaY systems to reoxidation treatment is consistent with the greater reactivities expected for small metal particles compared to larger aggregates. Raman spectroscopy and ^{129}Xe NMR provide complementary information that correlates well with hydrogen chemisorption and transmission electron microscopy results. These techniques represent important diagnostic probes of metal clustering processes in zeolites and, in combination, permit the influence of preparatory treatment conditions on metal guest distribution and stability to be established. Understanding the chemistry behind such metal dispersal processes is essential for proper control of metal cluster formation and distribution in molecular sieves. This has clear ramifications to heterogeneous catalysis and is important to the function and design of new quantum-effect materials as well.

ACKNOWLEDGMENTS

The authors thank Professor A. Pines, Dr. L. C. de Menorval, Dr. S. B. Liu, and Dr. R. Ryoo for helpful discussions and experimental support. This work was supported in part by the National Science Foundation under Grant NSF 83-14564. B. F. C. acknowledges the NSF-NATO Post-Doctoral and NSF Young Investigator Programs for financial support.

REFERENCES

1. Jacobs, P. A., "Carboniogenic Activity of Zeolites" Elsevier, Amsterdam, 1977.
2. Gallezot, P., *Catal. Rev. Sci. Eng.* **20,** 121 (1979).
3. "Proceedings of the Symposium on Zeolites, Szeged, Hungary, 1978" *Acta Phys. Chem.* **24** (1–2), 1–354 (1978).
4. Jacobs, P. A., *in* "Metal Microstructures in Zeolites" (P. A. Jacobs, N. I. Jaeger, P. Jíru, and G. Schulz-Ekloff, Eds.), p. 71. Elsevier, Amsterdam, 1982.
5. Stucky, G. D. and MacDougall, J. E., *Science* **247,** 669 (1990).
6. Dalla Betta, R. A. and Boudart, M., *in* "Proceedings of the Fifth International Congress on Catalysis, Miami, 1972" (J. W. Hightower, Ed.), Vol. 2, p. 1329. North-Holland, Amsterdam, 1973.
7. Gallezot, P., Alarcon-Diaz, A., Dalmon, J. A., Renouprez, A. J., and Imelik, B., *J. Catal.* **39,** 334 (1975).
8. Uytterhoeven, J. B., *Acta Phys. Chem.* **24,** 53 (1978).
9. Braun, G., Fetting, F., Haelsig, C. P., and Gallei, E., *Acta Phys. Chem.* **24,** 93 (1978).
10. Reagan, W. J., Chester, A. W., and Kerr, G. T., *J. Catal.* **69,** 89 (1981).
11. Exner, D., Jaeger, N., Möller, K., and Schulz-Ekloff, G., *J. Chem. Soc. Faraday Trans. 1* **78,** 3537 (1982).
12. Jaeger, N. I., Ryder, P., and Schulz-Ekloff, G., *in* "Structure and Reactivity of Modified Zeolites" (P. A. Jacobs, N. I. Jaeger, P. Jíru, V. B. Kazansky, and G. Schulz-Ekloff, Eds.), p. 299. Elsevier, Amsterdam, 1984.

13. Felthouse, T. R. and Murphy, J. A., *J. Catal.* **98,** 411 (1986).
14. Tzou, M. S., Jiang, H. J., and Sachtler, W. M. H., *React. Kinet. Catal. Lett.* **35,** 207 (1987).
15. Sachtler, W. M. H., Tzou, M. S., and Jiang, H. J., *Solid State Ionics* **26,** 71 (1988).
16. Tzou, M. S., Teo, B. K., and Sachtler, W. M. H., *J. Catal.* **113,** 220 (1988).
17. Jiang, H. J., Tzou, M. S., and Sachtler, W. M. H., *Appl. Catal.* **39,** 255 (1988).
18. Chmelka, B. F., de Menorval, L. C., Csencsits, R., Ryoo, R., Liu, S. B., Radke, C. J., Petersen, E. E., and Pines, A., *in* "Structure and Reactivity of Surfaces" (C. Morterra, A. Zecchina, and G. Costa, Eds.), p. 269. Elsevier, Amsterdam, 1989.
19. Ostgard, D. J., Kustov, L., Poeppelmeier, K. R., and Sachtler, W. M. H., *J. Catal.* **133,** 342 (1992).
20. Hong, S. B., Mielczarski, E., and Davis, M. E., *J. Catal.* **134,** 349 (1992); Mielczarski, E., Hong, S. B., Davis, R. J., and Davis, M. E., *J. Catal.* **134,** 359 (1992).
21. MacDougall, J. E., Eckert, H., Stucky, G. D., Herron, N., Wang, Y., Möller, K., Bein, T., and Cox, D., *J. Am. Chem. Soc.* **111,** 8006 (1989).
22. Ozin, G. A. and Özkar, S., *Adv. Mater.* **4,** 11 (1992).
23. Foger, K. and Anderson, J. R., *J. Catal.* **54,** 318 (1978).
24. Gallezot, P., *in* "Catalysis by Zeolites" (B. Imelik *et al.*, Eds.), p. 227. Elsevier, Amsterdam, 1980.
25. Ribeiro, F. R. and Marcilly, C., *in* "Proceedings of the Fifth International Symposium on Heterogeneous Catalysis, Varna, USSR" *Geterog. Katal. Trudy Mezhdunarounogd Sympoz.* **5,** 383, (1983).
26. Chmelka, B. F., Rosin, R. R., Went, G. T., Bell, A. T., Radke, C. J., and Petersen, E. E., *in* "Zeolites: Facts, Figures, Future" (P. A. Jacobs and R. A. van Santen, Eds.), p. 995. Elsevier, Amsterdam, 1989.
27. de Menorval, L. C., Fraissard, J. P., and Ito, T., *J. Chem. Soc. Faraday Trans. 1* **78,** 403 (1982).
28. Fraissard, J., Ito, T., de Menorval, L. C., and Spinguel-Huet, M. A., *in* "Metal Microstructures in Zeolites" (P. A. Jacobs, N. I. Jaeger, P. Jíru, and G. Schulz-Ekloff, Eds.), p. 179. Elsevier, Amsterdam, 1982.
29. Fraissard, J. P., Ito, T., and de Menorval, L. C., *in* "Proceedings of the Eighth International Congress on Catalysis, Berlin" Vol. 3, p. 25. Verlag-Chemie, Weinheim, 1984.
30. Boudart, M., Samant, M. G., and Ryoo, R., *Ultramicroscopy* **20,** 125 (1986).
31. Chmelka, B. F., Ryoo, R., Liu, S. B., de Menorval, L. C., Radke, C. J., Petersen, E. E., and Pines, A., *J. Amer. Chem. Soc.* **110,** 4465 (1988).
32. Petrakis, L., Springuel-Huet, M. A., Ito, T., Hughes, T. R., Chan, I. Y., and Fraissard, J., *in* "Proceeding of the Ninth International Congress on Catalysis, Calgary" (M. J. Phillips and M. Ternan, Eds.) Vol. 1 p. 348. Chemical Institute of Canada, Ottawa, 1988.
33. Ahn, D. H., Lee, J. S., Nomura, M., Sachtler, W. M. H., Moretti, G., Woo, S. I., and Ryoo, R., *J. Catal.* **133,** 191 (1992).
34. Yang, O. B., Woo, S. I., and Ryoo, R., *J. Catal.* **137,** 357 (1992).
35. Chmelka, B. F., Ph.D. dissertation, University of California, Berkeley, CA 94720 (1990).
36. Went, G. T., Oyama, S. T., and Bell, A. T., *J. Phys. Chem.* **94,** 4240 (1990).
37. Jameson, A. K., Jameson, C. J., and Gutowsky, H. S., *J. Chem. Phys.* **53,** 2310 (1970); Jameson, C. J., Jameson, A. K., and Cohen, S. M., *J. Chem. Phys.* **59,** 4540 (1973); Jameson, C. J., Jameson, A. K., and Cohen, S. M., *J. Chem. Phys.* **62,** 4224 (1975).
38. Csencsits, R. and Gronsky, R., *Ultramicroscopy* **23,** 421 (1987).
39. Bursill, L. A., Lodge, E. A., and Thomas, J. M., *Nature* **286,** 111 (1980).
40. Roozeboom, F., Robson, H. E., and Chan, S. S., *Zeolites* **3,** 321 (1983).
41. Dutta, P. K., Shieh, D. C., and Puri, M., *J. Phys. Chem.* **91,** 2332 (1987).
42. Cheng, C. P., Ludowise, J. D., and Schrader, G. L. *Appl. Spect.* **34,** 146 (1980).
43. Graham, G. W., Weber, W. H., McBride, J. R., and Peters, C. R. *J. Raman Spectros.* **22,** 1 (1991).
44. Emmett, P. H. and Brunauer, S., *J. Amer. Chem. Soc.* **59,** 1553 (1937).
45. Wilson, G. R. and Hall, W. K., *J. Catal.* **17,** 190 (1970).
46. Karnaukhov, A. P., *Kinet. Catal.* **12** (Part 2), 1345 (1971).
47. Gallezot, P., Mutin, I., Dalmai-Imelik, G., and Imelik, B., *Journal de Microsc. Spectrosc. Electron.* **1,** 1 (1976).
48. Homeyer, S. T. and Sachtler, W. M. H., *in* "Zeolites: Facts, Figures, Future" (P. A. Jacobs and R. A. van Santen, Eds.), p. 975. Elsevier, Amsterdam, 1989.
49. Ratnasamy, P., Leonard, A. J., Rodrique, L., and Fripiat, J. J., *J. Catal.* **29,** 374 (1973).
50. Burton, J. J., *Catal. Rev. Sci. Eng.* **9,** 209 (1974).
51. Gillet, M., *Surf. Sci.* **67,** 139 (1977).
52. Gallezot, P., Bienenstock, A. I., and Boudart, M., *Nouv. J. Chim.* **2,** 263 (1978).
53. Gordon, M. B., Cyrot-Lackmann, F., and Desjonquères, M. C., *Surf. Sci.* **80,** 159 (1979).
54. Via, G. H., Sinfelt, J. H., and Lytle, F. W., *J. Chem. Phys.* **71,** 690 (1979).
55. Moraweck, B., Clugnet, G., and Renouprez, A. J., *Surf. Sci.* **81,** L631 (1979).
56. Khanna, S. N., Bucher, J. P., Buttet, J., and Cyrot-Lackmann, F., *Surf. Sci.* **127,** 165 (1983).
57. Sachdev, A., Masel, R. I., and Adams, J. B., *J. Catal.* **136,** 320 (1992).

58. Gault, F. G., Garin, F., and Maire, G., *in* "Growth and Properties of Metal Clusters" (J. Bourdon, Ed.), p. 451. Elsevier, Amsterdam, 1980.
59. Domínguez, J. M. and Yacamán, M. J., *in* "Growth and Properties of Metal Clusters" (J. Bourdon, Ed.), p. 493. Elsevier, Amsterdam, 1980.
60. Gallezot, P., *Zeolites* **2,** 103 (1982).
61. Bergeret, G., Gallezot, P., and Imelik, B., *J. Phys. Chem.* **85,** 411 (1981).
62. Feeley, O. and Sachtler, W., *Appl. Catal.* **67,** 141 (1990).
63. Homeyer, S. T. and Sachtler, W. M. H., *Appl. Catal.* **54,** 189 (1989).
64. Burton, J. J., *J. Chem. Phys.* **52,** 345 (1970).
65. Fripiat, J. G., Chow, K. T., Boudart, M., Diamond, J. B., and Johnson, K. H., *J. Molec. Catal.* **1,** 59 (1975/76).
66. Ghandhi, S. K., "VLSI Fabrication Principles." Wiley, New York, 1983.
67. Wang, T., Lee, C., and Schmidt, L. D., *Surf. Sci.* **163,** 181 (1985).
68. Cates, G. D., Benton, D. R., Gatzke, M., Happer, W., Hasson, K. C., and Newbury, N. R., *Phys. Rev. Lett.* **65,** 2591 (1990).
69. Raftery, D., Long, H., Meersmann, T., Grandinetti, P. J., Reven, L., and Pines, A., *Phys. Rev. Lett.* **66,** 584 (1991).